

Effects of decimetre-scale surface roughness on L-band Brightness

Temperature of Sea Ice

Maciej Miernecki^{2,1}, Lars Kaleschke^{3,1}, Nina Maaß¹, Stefan Hendricks³, and Sten Schmidl Søbjaerg⁴

¹Institute of Oceanography (IfM), University of Hamburg, Bundesstr. 53, 20146 Hamburg Germany

²Centre d'Etudes Spatiales de la Biosphère (CESBIO), 18 avenue Edouard Belin bpi 2801, 31401 Toulouse Cedex 9, France

³Alfred Wegener Institute, Helmholtz Centre for Polar and Marine Research, Bremerhaven, Bussestrasse 24, 27570

Bremerhaven, Germany

⁴Technical University of Denmark, Ørstedes Plads, 2800 Kgs. Lyngby Danmark

Correspondence: Maciej Miernecki (maciej.miernecki@cesbio.cnes.fr)

Abstract. Sea ice thickness measurements with L-band radiometry ~~is a technique which allows~~ allow for daily, weather-independent monitoring of the polar sea ice cover. The sea-ice thickness retrieval algorithms ~~rely-rely~~ on the sensitivity of the L-band brightness temperature to sea-ice thickness. In this work, we investigate the decimetre-scale surface roughness as a factor influencing the L-band emissions from sea ice. We ~~used-use~~ an airborne laser scanner to construct a digital elevation model of the sea ice surface. We ~~found-find~~ that the probability density function of surface slopes is exponential for a range of degrees of roughness. Then we ~~applied-apply~~ the geometrical optics, ~~bounded-bound~~ with the Microwave L-band LAYERed Sea ice emission model in the Monte Carlo simulation to simulate the effects of surface roughness. According to ~~this-these~~ simulations, the ~~most-affected-by-surface-roughness-is-the~~ vertical polarization around Brewster's angle ~~,where the decrease in brightness temperature can reach~~. The vertical is most affected by decimetre-scale surface roughness with brightness temperature decreasing up to 8 K. The horizontal polarization for the same configuration exhibits a 4 K increase. The near-nadir angles are little affected, up to 2.6 K decrease for the most deformed ice. These result indicate that the current operational sea ice thickness retrieval algorithm using the near-nadir L-band is marginally affected by omission of the surface roughness. Overall the effects of large-scale surface roughness can be expressed as a superposition of two factors: the change in intensity and the polarization mixing. The first factor depends on surface permittivity, the second shows little dependence

on it. The sensitivity analysis indicates that snow cover impacts the brightness temperature to a greater extent than surface roughness. Comparison of the brightness temperature simulations with the radiometer data does not yield definite results.

Copyright statement. TEXT

1 Introduction

5 The L-band brightness temperature (T_B) is sensitive to sea ice thickness, ~~a feature that~~. This feature is used for sea ice thickness retrieval from L-band T_B (over thin ice, $<$) ~~Tian-Kunze et al. (2014), Huntemann et al. (2014), Kaleschke et al. (2016)~~ 1.5 m (Tian-Kunze et al., 2014; Huntemann et al., 2014; Kaleschke et al., 2016). Several factors influence ~~the T_B measured measurements~~ over ice-covered regions, among them: ice concentration, ice temperature, snow cover ~~and surface roughness are among them~~ Maaß et al. (2013), Ulaby, F. T. and Long, D. G. et al. (2014), sea ice surface roughness and the shape of the interfaces between the snow and ice layers (Maaß et al., 2013; Ulaby, F. T. and Long, D. G. et al., 2014).

Here, we investigate the effect effects of surface roughness on the L-band T_B , ~~a factor that so far has not been specifically the large scale roughness. So far this factor is not~~ included in the modeling of ~~the~~ sea ice emissions ~~and~~ in operational sea ice thickness retrieval. ~~In the theory of electromagnetic scattering~~, Electromagnetic scattering theory assumes that the roughness of a random surface is characterized by statistical parameters ~~such as the including~~ standard deviation of surface height (σ_z), and ~~the~~ correlation function ($R(\xi)$) measured in units of wavelength Ulaby, F. T. and Long, D. G. et al. (2014). ~~The~~ (Ulaby, F. T. and Long, D. G. et al., 2014). These roughness statistical parameters are derived from measurements of surface elevation (z), ~~from which the roughness statistics are drawn, are~~ conducted with altimeters that are characterized by their accuracy (δ) and sampling distance (Δx). ~~Thus~~ As usual, the measurement method has an impact on the ~~result outcome, in this case~~ by filtering out both high and low spatial frequencies of the surface roughness. ~~The sea~~ Sea ice elevation measurements obtained from ~~air-borne altimeters Ketchum (1971), Dierking (1995)~~, airborne altimeters (Ketchum, 1971; Dierking, 1995) and supplemented with terrestrial laser scanners Landy et al. (2015), (Landy et al., 2015) draw a picture of sea ice roughness as a multi-scale feature covering several orders of magnitude from large floes and pressure ridges ~~of tens and hundreds meters (from tens to hundreds meters)~~ to frost flowers and small ripples ~~of centimeters to millimeters scales (in the centimeter to millimeter scale)~~. The incident wavelength radiation of a given wavelength (λ) reacts differently with individual components of the superimposed roughness Ulaby, F. T. and Long, D. G. et al. (2014). ~~The roughness scales much greater than the electromagnetic wavelength (λ) alter the local incidence angle. On the other of many scales (Ulaby, F. T. and Long, D. G. et al., 2014)~~.

At small end of the roughness spectrum ~~, i.e.~~ when the change of ~~the surface elevation Δz across sampling distance Δx surface elevation over sampling distance ($\Delta z / \Delta x$)~~ is much smaller than λ , ~~the roughness stays unnoticed ($\Delta z / \Delta x \ll \lambda$), the surface roughness is negligible. It means that the angular characteristics of scattered radiation are the same as for the secular surface.~~ As a rule of thumb, ~~the~~ Δx should be smaller than 0.1λ Dierking (2000) (Dierking, 2000). Sea ice roughness measurements with terrestrial lidar carried out by Landy et al. (2015) show that Landy et al. (2015) show that standard deviation of

surface height σ_z ranges from ~~to~~ 0.001 m to 0.0064 m, after high-pass filtering (cut off at 4 m^{-1} , $\Delta x = 0.002 \text{ m}$). These results indicate that, according to the Fraunhofer's smoothness criterion ($\sigma_z < \lambda/32 \cos \theta$, where θ is the angle of incidence), most sea ice types (except artificially grown frost flowers) ~~;~~ can be treated as a smooth surface for L-band at scales lower than ~~;~~ 0.25 m.

In this study we ~~will~~ focus on the other side of the roughness spectrum ~~;~~ i.e. the large-scale surface roughness of sea ice
5 ~~($\Delta z / \Delta x \gg \lambda$). In this case, changes in surface elevation are not negligible and their alter the local incidence angle (θ_i). Studies of surface scattering~~ ~~with numerical simulations conclude that a by~~ Lawrence et al. (2011, 2013) conclude that region of $8\lambda \times 8\lambda$ is ~~large enough to represent~~ sufficient to model small-scale ~~surface roughness in scattering models~~ Lawrence et al. (2011) ~~;~~ Lawrence et al. (2013). Hereby ~~roughness. Here,~~ we assume that ~~scales greater than 8λ at larger spatial scales (larger than~~ $8\lambda \times 8\lambda$) the surface roughness can be characterized in terms of geometrical optics (GO). ~~In GO the surface is represented;~~
10 for sea ice with $\epsilon_{ice} = 4.1$, $\lambda_{ice} = \lambda / \sqrt{\epsilon_{ice}} \approx 0.1 \text{ m}$.

GO approximation describes the surface as a set of facets Ulaby, F. T. and Long, D. G. et al. (2014) (Ulaby, F. T. and Long, D. G. et al., 2014). This approach was applied in modeling of ~~for modeling~~ the effective emissivities of mountainous terrain Matzler and Standley (2000) ~~;~~ as well as other surfaces such as the one of the sea Prigent and Abba (1990) (Matzler and Standley, 2000) and ocean surface (Prigent and A
15). The latter study involved probability distribution of slopes in ~~across-~~ crosswind and downwind directions. A similar method was used in the context of sea ice to assess the uncertainties caused by ~~the~~ roughness in sea ice concentration products derived from passive microwaves Stroeve et al. (2006). ~~(Liu et al., 2014)~~ (Stroeve et al., 2006). Liu et al. (2014) measured ice surface slopes and other roughness statistics in the Bohai Sea, ~~but their~~. Their result was obtained with linear (1-D) scans under the assumption of isotropic roughness characteristics. The study by ~~(Beckers et al., 2015)~~ Beckers et al. (2015) has demonstrated that the statistics of sea ice roughness (mean z , σ_z , kurtosis and skewness) obtained from 1-D altimeter and 2-D laser scanner
20 converge, provided on the condition that the surface is not strongly heterogeneous. Nonetheless, the 1-D altimeter data cannot properly represent the spatial orientation of surface facets, ~~which~~. The surface facet orientation is characterized by both the slope (α) and the azimuthal angle in which it is facing (γ). ~~In this work,~~

In this paper we address the ~~issue of surface slope orientation by extracting this information from the~~ knowledge gap regarding the influence of large-scale surface roughness on L-band T_B . Section 2 introduces the experimental data collected
25 during SMOSice2014 campaign (section 2.1). Among them are the airborne laser scanner elevation measurements for surface roughness characterization and EMIRAD2 L-band radiometer T_B measurements. The surface elevation measurements are used to construct a digital elevation model (DEM) ~~obtained with 2-D measurements. Then we identify the spatial scales at which sea ice can be treated as isotropic in terms of surface slopes orientation. The surface roughness statistics are subsequently used in~~ combination with of sea ice surface. From the DEM we derive the facet surface slopes and their orientation. In section 2.2 we
30 analyze the statistics of the facet orientation. Based on facet orientation statistics, we derive a parametrization of the probability distribution function of surface slopes (PDF_α), that will serve as surface roughness representation in T_B simulations.

For the simulation of the sea ice T_B we use the MICrowave L-band LAyered Sea ice emission model (MILLAS) ~~to simulate the brightness temperature over~~ (Maaß et al., 2013). In section 2.4 we show how we integrate the surface roughness statistics (PDF_α) with MILLAS using geometrical optics.

The three key results of this study, namely (a) the T_B simulations for sea ice with different degrees of roughness. Finally, we compare surface roughness (b) the sensitivity study of the model (c) comparison of the EMIRAD-2 radiometer measurements with modeled T_B with and without roughness parametrization are subsequently presented and discussed (section 3).

Section 4 discusses the implications of this study for current and future L-band missions.

5 2 Materials and Methods

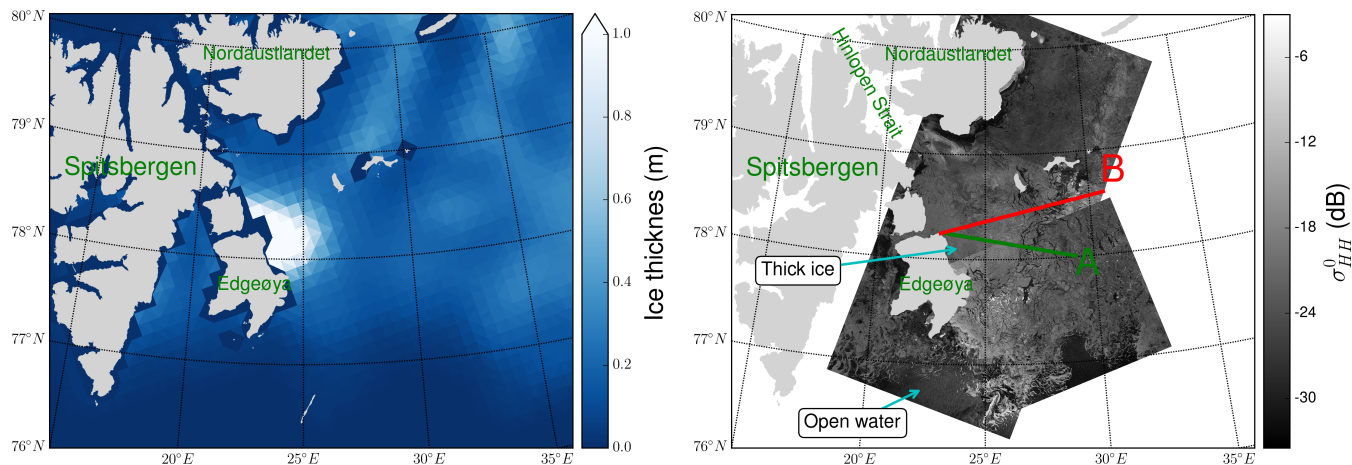
In this section we present the SMOSice2014 campaign that is the key dataset of this study. Section 2.2 presents the sea ice surface roughness measurements in the context of geometrical optics. Section 2.3 presents the sea ice emission model that we used.

2.1 SMOSice2014 Campaign

10 The SMOSice2014 campaign took place between March 21, 2014 and March 27, 2014 in the area between Edgeøya and Kong Karls Land, east of Svalbard. A broader description of the campaign was made by (Kaleschke et al., 2016),(Hendricks et al., 2014) Hendricks et al. (2014) and Kaleschke et al. (2016) described the campaign extensively. In this study we analyzed the data acquired during the flights on March 24/26, at 26. From this point, we evoke just onwards we focus solely on the parts relevant to the presented work.

15 2.2 SMOSice2014 Campaign

In the period preceding the experiment ,from late January until early March ,the meteorological conditions in the region deviated strongly from the climatological means. The air temperature measured at Hopen Island meteorological station was on average 9 to 12°C higher than the climatological value for the period 1961-1990 Strübing and Schwarz (2014) (Strübing and Schwarz, 2014). Prevailing southerly winds pushed sea ice against the coasts of Nordaustlandet and into Hin-
20 lopen Strait, leaving a small strip of compacted ice along the coasts of Edgeøya. When sea ice returned with southerly drift in early March it set the scene, the scene was set for the experiment. The thickest, most deformed ice was located in the western part of the studied region with a gradual decrease in thickness eastwards, where thin newly-formed ice was dominant. This pattern can be observed in the SMOS sea ice thickness product displayed in Figure 1a. In this work, we analyze only focus on the data from the low altitude flight at ,as it has the 70 m, because it is the data with highest spatial resolution of the Airborne
25 Laser Scanner (ALS) among all the flights. Also, we limit the analysis The analysis was further reduced to the 24th of March, it is due to the fact that the region covered on 26th March had a discontinuous ice cover and a large scale swell was interfering with the surface elevation measurements. On March 24, the Polar 5 research aircraft of the Alfred Wegener Institute (Bremerhaven, Germany), undertook measurement flights starting from the eastern coast of Edgeøya, along the lines marked in red and green on Figure 1b. The figure also shows TerraSAR wide swath scenes, taken in the region. Flight A was made between
30 10:05 and 10:41 UTC, flight B occurred from 11:25 to 12:07 UTC. A-The set of instruments was mounted on the aircraft ; including included an aerial camera to visually register the ice conditions, the Heitronics KT19.85 pyrometer for surface tem-



(a) Sea ice thickness on March 24 2014, derived from SMOS. The SMOS sea ice thickness product with a resolution of 40 km is presented on a 15 km grid. An aggregation of thick ice (>1 m) is visible along the Edgeøya's eastern coast.

(b) Sea ice conditions in the flights-flight region on March 24. The TerraSAR-X wide swath mode (HH polarization), with frames taken at 05:35 UTC and 14:58 UTC. The aircraft tracks are marked in green - A at 10:05-10:41 UTC and red - B at 11:25-12:07 UTC.

Figure 1. The region of SMOSice2014 Campaign.

perature measurements, the L-band radiometer EMIRAD-2, and the Airborne Laser Scanner (ALS) for high-resolution surface elevation measurements.

2.2 EMIRAD-2 Radiometer

2.1.1 EMIRAD-2 Radiometer

- 5 The EMIRAD-2 L-band radiometer, (developed by DTUSpace,) is a fully polarimetric system with advanced radio frequency interference (RFI) detection features Søbjaerg et al. (2013) (Søbjaerg et al., 2013). The setup mounted on the aircraft consists of two Potter horn antennas, one nadir pointing, one side looking at 45° incidence angle. The antennas' footprints dimensions for a flight altitude are approximately and by, respectively. As the aircraft flew at the altitude of 70 m, the footprint of each antenna was 60 m × 90 m for the nadir pointing antenna, and 70 m × 90 m for the side looking antenna. The receiver has a sensitivity of for integration time. During all flight operations navigation data are collected and used's sensitivity is 0.1 K for a 1 s integration window. Along with the L-band measurements, navigation data was collected as to transform the polarimetric brightness temperature into the Earth reference frame Hendricks et al. (2014) (Hendricks et al., 2014). The EMIRAD-2 data have been was screened by evaluating kurtosis, polarimetric Balling et al. (2012) (Balling et al., 2012), and brightness temperature (T_B) anomalies, this revealed. The screening showed RFI contamination for up to 30% RFI contamination. When subtracting of the samples. After subtracting of the mean value of the RFI-flagged data from the mean value of the full data a difference of typically a few Kelvin is present for a side looking horn and typically for the nadir-looking horn. Data analysis, we found a 10 K difference for the nadir-looking horn, while the difference was non significant for the side looking horn.

The analysis of the T_B during the "wing wags" calibration maneuvers further revealed a 20 K offset relative to the nadir nadir-looking vertical channel caused by a continuous wave signal from the camera that was mounted on the airplane to obtain visual images. ~~This contamination could not be detected by the RFI filters but the~~ The analysis concludes a purely additive characteristic ~~and allowed a bias correction Hendricks et al. (2014)~~ that allowed for bias correction (Hendricks et al., 2014).

5 In this study, we use the data pre-processed by the DTU-team. The radiometer data was RFI cleaned and bias-corrected and validated using aircraft wing wags and nose wags over open ocean ~~Hendricks et al. (2014)~~ (Hendricks et al., 2014).

2.2 Airborne Laser Scanner

~~The~~

2.1.1 Airborne Laser Scanner

10 In this study, the ALS (Riegel VQ-580 laser scanner is essential to this study, as it is used for measuring) has two purposes: (1) to measure the surface elevation ~~from which sea ice thickness is estimated, as well as for subsequent estimation of the ice thickness~~ and (2) to characterize the surface topography ~~characterized~~. The near-infrared laser (wavelength 1064 nm) is measuring snow and ice elevation with the accuracy and precision of ~~. During the flights it was operating with pulse repetition frequency of,~~

15 measuring the surface elevation in cross-track linear scan in the 0.0025 m. Across-track and along-track elevation measurements were obtained every 0.25 m and 0.50 m, respectively. These sampling characteristics resulted from the combination of the flight altitude (70 m) and the setup of the ALS (pulse repetition rate of 50 kHz, cross track range of ± 30 degrees. ~~Such configuration at the flight altitude of resulted in across-track and along track sampling of and, respectively).~~ The field of view of the radiometer

side-looking antenna was only partially covered by the ALS scans. Nonetheless we assume that the roughness characteristics measured by ALS are representative for both antennae field of views. The data were calibrated and geo-referenced to the 20 WGS84 datum. Further processing involved manual classification of tie points in leads in order to obtain ~~the~~ local sea level and sea ice free-board ~~Hendricks et al. (2014)~~ (Hendricks et al., 2014). The geo-referenced surface elevations are used to compute surface roughness statistics. The elevation data ~~are is~~ interpolated to a regular by 0.5 m by 0.5 m grid to form a digital elevation model (DEM) of the sea ice surface. The DEM serves to derive surface slopes orientation. ~~The ALS free-board data is used to estimate the-~~

25 The typical set of data required to estimate sea ice thickness ~~. The estimation method uses the assumption of hydro-static equilibrium. In order to derive the sea ice thickness, consists of (a) the densities of water and ice must be known, as well as,~~ and (b) the snow load, ~~classically~~ described by snow density and snow thickness. ~~Unfortunately, during the flights the snow radar-~~

30 The water, ice, and snow densities retained are 1027 kg/m³ (water) and 917 kg/m³ after Ricker et al. (2014), and 300 kg/m³ after Warren et al. (1999).

Snow thickness was meant to be provided by the onboard snow radar, however the equipment was still in ~~the test phase of~~ development, therefore we decided not to use this data. In order to tackle the problem of the lack of the snow thickness data, we follow ~~(Kaleschke et al., 2016)~~ and assume an approximation formula used by ~~(Yu and Rothrock, 1996) and (Mäkynen et al., 2013)~~

~~–which sets test phase at the time of the experiment. As a workaround, we followed Kaleschke et al. (2016) and used the approximations found in Yu and Rothrock (1996) and Mäkynen et al. (2013)) that set the snow thickness to 10% of the sea ice thickness. As for the respective densities, we assume the water density as , ice density after (Rieker et al., 2014) and snow density after (Warren et al., 1999)~~

5 The actual estimate of sea ice thickness was built on the hydro-static equilibrium assumption, the above data, and the ALS’s free-board data.

2.2 Sea Ice **Brightness Temperature Simulation**Surface Roughness

For the simulation of sea ice brightness temperature (T_B) we use the Microwave L-band Layered Sea ice emission model described by (Maaß et al., 2013), further referred to as MILLAS. This model is based on the radiative transfer model of (Burke et al., 1979) (who used it for soils), with infinite half-space of seawater covered with layers of sea ice, snow and a top semi-infinite layer of air. ~~In contrast to~~ In this subsection we will analyze the data from the airborne laser scanner (ALS) that we presented in section 2.1.1. We use the ALS data to measure the decimetre-scale surface roughness. The ALS is a laser instrument that measures the distance to the surface. That surface is most likely to by snow laying on the original model of (Burke et al., 1979) and its usage by (Maaß et al., 2013), the current version of MILLAS takes into account multiple reflections at the layer boundaries. The MILLAS model describes the brightness temperature above snow-covered sea ice as a function of temperature and permittivity of the layers. The water permittivity depends mainly on the water temperature and salinity Klein and Swift (1977) ~~–Ice permittivity can be approximately described as a function of brine volume fraction Vant et al. (1978), which depends on ice salinity and the densities of the ice and brine Cox and Weeks (1982), which in turn depend mainly on ice temperature. The permittivity of dry snow can be estimated from its density and temperature Tiuri et al. (1984). In the simulation setup, the ice and water salinity are kept constant. Furthermore, we assume that the system is in thermal equilibrium, and the water beneath ice. The relief of the ice is at the freezing point. In this configuration, the T_B is simulated as a function of ice thickness (d_{ice}), snow thickness (d_{snow}) and surface temperature (T_{surf}). In our setup, the snow is assumed to be dry with a density of , which is the average snow density value for December Arctic measurements from 1954-91 Warren et al. (1999). The TB simulations are only slightly sensitive to snow density, see Figure 3 in (Maaß et al., 2013). The permittivities of snow and ice are linked to their temperature. The temperature profiles within snow and ice are assumed to be continuous and linear. The values for the ice and snow thermal conductivity are taken from (Yu and Rothrock, 1996), (Untersteiner, 1961). As the optimization of the emission model lays beyond the scope of this work, we use the simplest setup variant of the MILLAS model consisting of a single layer of ice covered with a single layer of snow therefore modified by snow cover. During the SMOSice2014 campaign the snow measurements were unavailable. We assume that snow cover is a plane-parallel layer over sea ice. This assumption do not accounts for snow dunes and drifts that may form on the ice. The implications of snow thickness on the radioactive transfer modeling are discussed in the section presenting the sensitivity analysis (section 3.2).~~

2.3 Sea Ice Surface Roughness

We used the ALS data from SMOSice2014 to measure the decimeter-scale surface roughness. In the context of the radiation transfer, the surface roughness is characterized in relation to incident wavelength. The ALS spatial resolution of along-track spatial sampling of 0.5 m is a few times larger than the L-band wavelength in sea ice ($\lambda_{ice} = \lambda / \sqrt{\epsilon_{ice}} \approx 0.1 \text{ m}$), which makes it suitable to measure the large-scale roughness, the part of the roughness spectrum where geometrical optics GO can be used to approximate the path of radiation. In the first step, we identify the ice with different degree of surface roughness. For that, we divide the flight tracks into one-second sections (approximately 70 m-70 m long), large enough to cover the entire nadir radiometer footprint, and we make-build a histogram of the standard deviations of surface heights computed from-for these sections. The number of bins in the histogram is set according to the formula: $N_{bins} = 5 \log_{10}(N_{data})$, after Panofsky and Brier (1958) Panofsky and Brier (1958). We decided on standard deviation as the criterion for defining the roughness classes, as it is widely used to characterize surface roughness from elevation profiles, and. Also, unlike visual interpretation of the aerial photography of sea ice it does not introduce personal biases. The resulting histogram in Figure 2, shows the sea ice roughness classes as histograms bins. No strips within the lowest standard deviation of surface height were found, that is probably due to the fact that no refrozen lead of the scale of 70 m was found or the ALS laser signal was not reflected back from the surface resulting in a missing data.

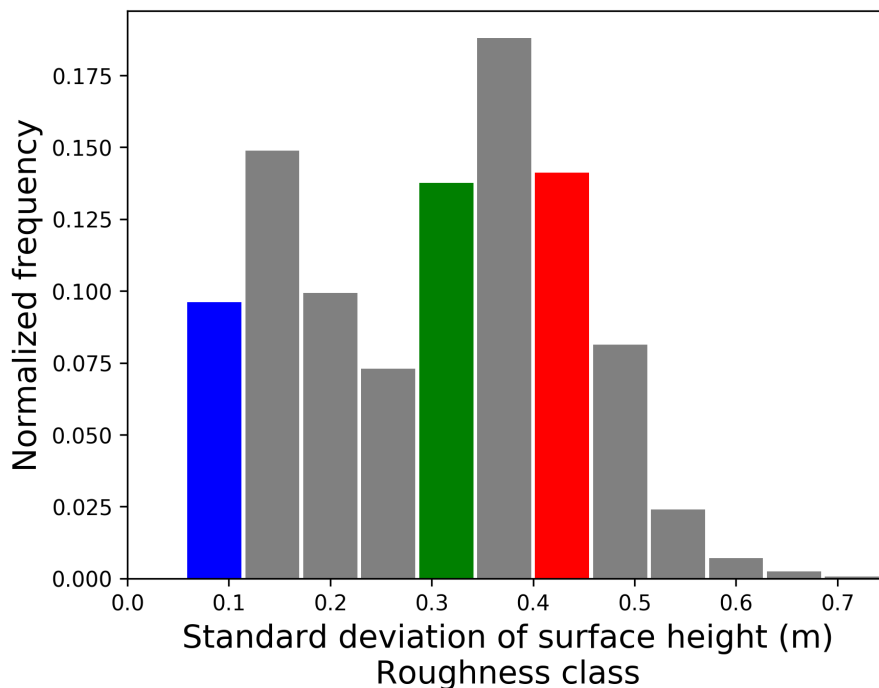


Figure 2. Histogram of the standard deviation of surface heights computed from 70 m flight strips, bins define the roughness classes of sea ice. Examples for three roughness classes "smooth", "medium rough" and "rough" are marked in colors blue, green and red, respectively.

15 In the second step, we interpolate the ALS elevation measurements to a regular 0.5 m grid in order to form a digital elevation model (DEM) of the sea ice surface. The sea ice surface in the DEM is represented as a set of triangular facets. Each facet

orientation in the 3D Cartesian space (For simplicity we assume the base vectors $\hat{x}, \hat{y}, \hat{z}$ to be aligned with the aircraft principal axis, so \hat{x} points to the flight direction), is described by two angles: the facet slope α ($0 \leq \alpha < \pi$) and the facet azimuthal direction γ ($-\pi \leq \gamma < \pi$). Therefore, the i -th facet local normal vector is described by:

$$\hat{n}_i = -\hat{x} \sin(\alpha_i) \cos(\gamma_i) - \hat{y} \sin(\alpha_i) \sin(\gamma_i) + \hat{z} \cos(\alpha_i) \quad (1)$$

5 In the third step, we compute the normal vectors and their orientations for the individual facets. This is done for all roughness classes. We found that the azimuthal orientation angle γ does not show any preferred directions within any given roughness class. ~~Local~~ However, local elongated structures such as pressure ridges along the coast might have dominant directions of the slopes, however, our study concluded that in the entire region, the distribution of azimuthal orientation angle γ is isotropic at scales greater than (Not shown). Therefore for the purpose of this study, we assume the distribution of ~~to be random and isotropic. As far as the facet slope is concerned, for-~~ In the next subsections we present the analysis of the two angles characterizing the facet: azimuthal direction and surface slope.

2.2.1 Facet azimuth orientation

In the previous section we used the DEM to calculate the vectors normal to the surface facets. In this subsection we analyse the orientations of facet azimuths. In order to evaluate the distribution of the facet azimuths, we define parameter f_R (eq. 2). This parameter is calculated from a histogram of azimuth orientation. In eq. 2 the denominator is the total number of samples under consideration expressed as the number of angular bins multiplied by the mean number of samples per bin. The numerator is a sum of the differences between the mean number of samples per bin and the actual number of samples in each bin. There are 36 bins. The number of bins was determined with $N_{bins} = 5 \log_{10}(N_{data})$ considering the maximal number of samples in 25 km flight track.

20 The f_R parameter equals to zero for the perfectly uniform distribution, in which case the number of counts in each bin (n_i) equals to a mean number of counts (μ). The f_R parameter reaches its maximum value of $f_{Rmax} = 2 - 4/N_{bins}$ when the slopes are aligned, i.e. grouped in two bins.

$$f_R = \frac{\sum_i^{N_{bins}} (|n_i - \mu|)}{N_{bins} \mu}, \quad \mu = \frac{1}{N_{bins}} \sum_i^{N_{bins}} n_i \quad (2)$$

25 To evaluate f_R we selected 1000 random 15 km samples from the flight tracks. The analysis of the samples shows that the deviation from the uniform distribution decreases sharply with increasing distance over first kilometer (figure 3). For distance along the sample greater than 4.3 km the curve flattens at value of $f_R = 0.05$ in 90% of the samples. We assume that at scales greater than 4.3 km marked by vertical dashed line on figure 3 slope orientations do not have a preferential direction beyond

natural variability. This distance corresponds to approximately 60 s sections. In figure 3 the average value of f_R is marked as thick red line. Several sample profiles are plotted in gray lines to illustrate the variability.

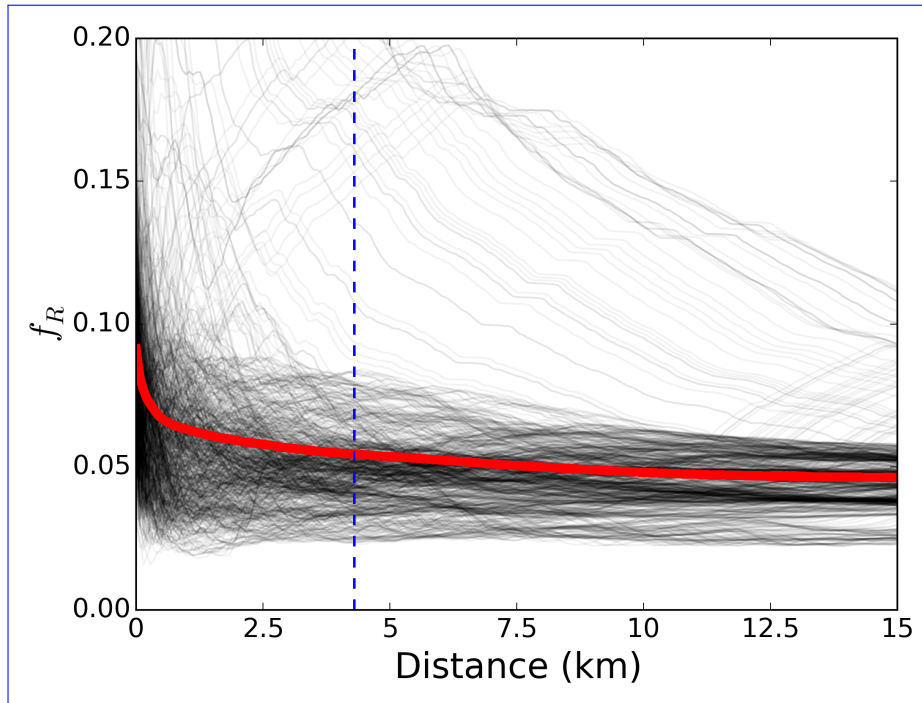


Figure 3. The f_R parameter illustrating the deviation from the uniform azimuth distribution along 1000 randomly selected samples. The average value of f_R is marked as thick red line. The 4.3 km threshold of uniform distribution is marked by blue dashed line.

2.2.2 Facet slope angle

Section 2.2.1 looked at the the azimuthal orientation of surface facets. This section focuses on the analysis of facet slopes.

- 5 For all roughness classes we observe a similar probability density function (PDF) with of surface slopes. The PDFs have a maximum at zero and a gradual decline in the likelihood of encountering the steeper slopes. Figure 4 shows the PDF_α in a logarithmic scale for the three distinct roughness classes: smooth $0.05 \text{ m} < \sigma_z < 0.11 \text{ m}$ (in blue), medium rough $0.28 \text{ m} < \sigma_z < 0.34 \text{ m}$ (in green) and rough $0.45 \text{ m} < \sigma_z < 0.51 \text{ m}$ (in red).

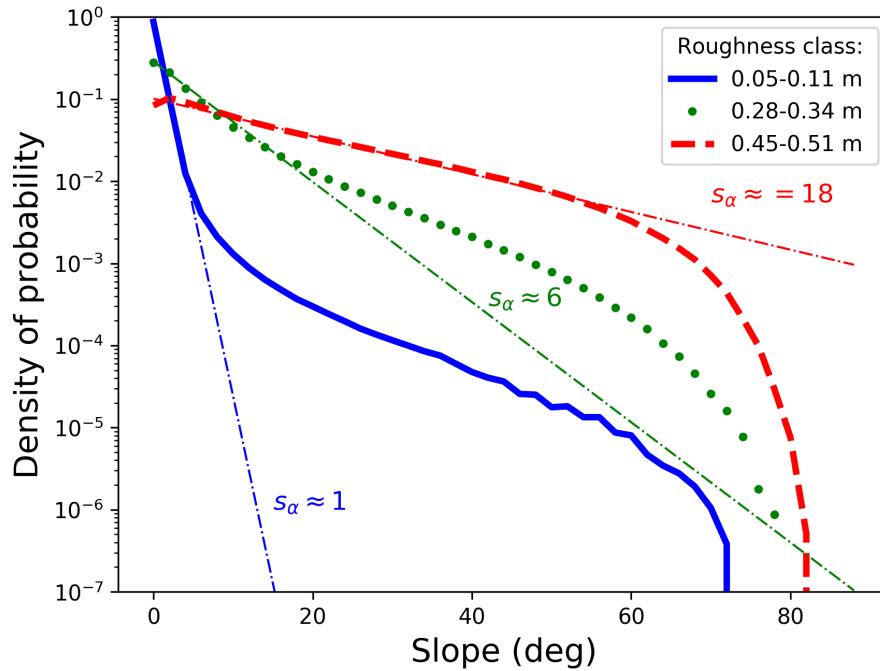


Figure 4. Density of probability of surface slopes in logarithmic scale for three roughness classes: smooth $0.05\text{ m} < \sigma_z < 0.11\text{ m}$ (in blue), medium rough $0.28\text{ m} < \sigma_z < 0.34\text{ m}$ (in green) and rough $0.45\text{ m} < \sigma_z < 0.51\text{ m}$ (in red). The exponential fits to the respective curves are marked in thin color dotted lines.

We decide to approximate the PDF of surface slopes with an exponential curve:

$$PDF_{\alpha} = \underline{A} \underline{C}_{norm} \exp(-(\alpha/s_{\alpha})), \quad (3)$$

where $\underline{A} \underline{C}_{norm}$ is the normalization constant and s_{α} is the “geometrical-slope roughness parameter”. For some roughness classes other functions can be fitted more accurately, however the exponential function performs well in all roughness classes and because it is a one-parameter function (with Figure 4 presents the data and the exponential approximations. The log scale is very relevant because it becomes obvious that the chances of encountering steep slopes are getting slimmer the higher the slope angle. Consequently, it makes sense that the approximation functions misfit the observations at high slope angles as it is irrelevant to fit an approximation there. As s_{α} (defining it's shape) is the only parameter of the approximation function, it is strait forward to interpret in terms of roughness — PDF_{α} — relation. descriptive of the surface roughness.

Figure 5 shows the relation between s_{α} and the standard deviation of surface heights corresponding to the roughness classes defined above. The error bars manifest represent the uncertainty associated with each data point. The large uncertainty for the very rough ice is caused by a relatively small number of data samples from such regions. Very rough ice has large uncertainty, because the number of samples was small (classes with $\sigma_z > 0.6\text{ m}$, accounted for less than 75 s of flight, out of total 78 min).

The quadratic relation is holding well for ice with up to 0.5 m standard deviation of surface heights. The red dashed line marks equation of the fitted curve $s_\alpha = 0.9009\sigma_z^2 + 0.0263\sigma_z + 0.0024$ is: $s_\alpha = 51.61\sigma_z^2 + 1.50\sigma_z + 0.14$

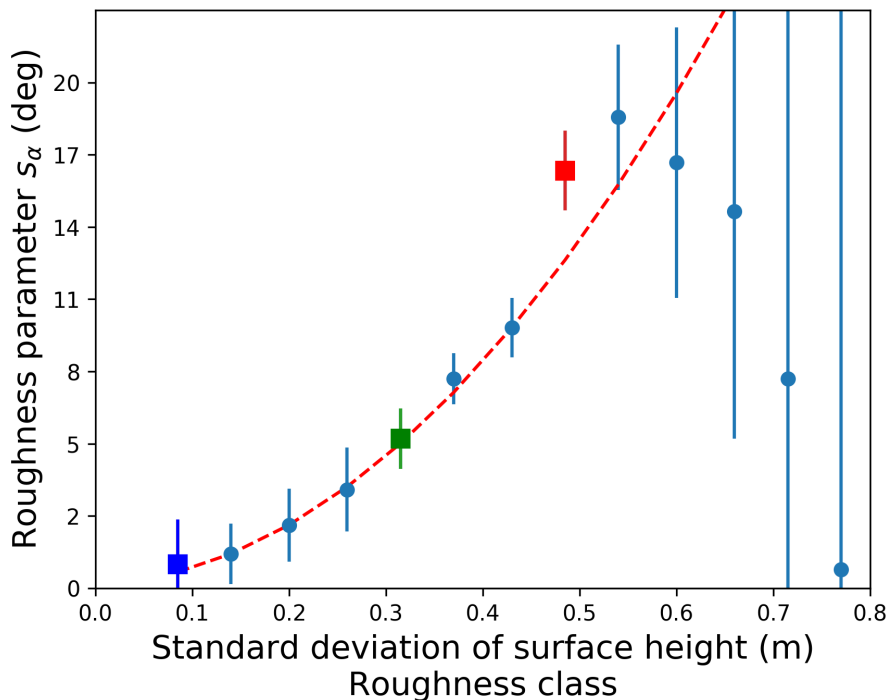


Figure 5. Surface roughness parameter s_α describing the probability distribution of surface slopes. Error bars are inversely proportional to the uncertainties, Inverse of the number of data points in each roughness class. The "smooth", "medium rough" and "rough" classes are marked in colors blue, green and red, respectively. The red dashed line marks the fitted curve.

2.3 Sea Ice Brightness Temperature Simulation

In this subsection we present the emission model for simulating the sea ice brightness temperature (T_B). We use the MICrowave
5 L-band LAYered Sea ice emission model described by Maaß et al. (2013), further referred to as MILLAS. This model is based
on the radiative transfer model of Burke et al. (1979)(who used it for soils), with infinite half-space of seawater covered with
layers of sea ice, snow and a top semi-infinite layer of air. In contrast to the original model of Burke et al. (1979) and its usage
by Maaß et al. (2013), the current version of MILLAS takes into account multiple reflections at the layer boundaries. The
multiple reflections are expressed as subsequent terms of a geometric series. The summation over series stops when terms of
10 the series contribute less than a given threshold to the total (in following calculations the threshold was set to 0.001). MILLAS
describes the brightness temperature above snow-covered sea ice as a function of temperature and permittivity of the layers.
The water permittivity depends mainly on the water temperature and salinity (Klein and Swift, 1977). Ice permittivity can
be approximately described as a function of brine volume fraction (Vant et al., 1978), which depends on ice salinity and the
densities of the ice and brine (Cox and Weeks, 1982), which in turn depends mainly on ice temperature. We set the ice salinity

Table 1. Brightness temperature simulation setup of the MIcrowave L-band LAyered Sea ice emission model (MILLAS).

	<u>Parameter</u>	<u>Value</u>
Snow	<u>surface temperature</u>	<u>measured (KT19)</u>
	<u>snow wetness</u>	<u>0%</u>
	<u>snow density</u>	<u>300 kg/m³</u>
	<u>snow thermal conductivity</u>	<u>0.31 W/(mK)</u>
Ice	<u>ice thermal conductivity</u>	<u>2.034 W/(mK) + 0.13 W/m · S_{ice} (g/kg)/T_{ice} (K)</u>
	<u>ice salinity</u>	<u>4 g/kg</u>
Water	<u>water salinity</u>	<u>33 g/kg</u>
	<u>water temperature</u>	<u>271.2 K</u>

to 4 g/kg which is a mean value for first year ice determined by Cox and Weeks (1974). The permittivity of dry snow can be estimated from its density and temperature (Tiuri et al., 1984). In the simulation, the ice and water salinity are kept constant (see Table 1), furthermore we assume that the system is in thermal equilibrium, and that the water beneath the ice is at the freezing point. In this configuration, the T_B is simulated as a function of ice thickness (d_{ice}), snow thickness (d_{snow}) and surface temperature (T_{surf}). In our setup, the snow is assumed to be dry with a density of 300 kg/m³, that is the average snow density value for December Arctic measurements from 1954-91 Warren et al. (1999). The T_B simulations are only slightly sensitive to snow density, see Figure 3 in Maaß et al. (2013). The permittivities of snow and ice are linked to their temperature. The temperature profiles within snow and ice are assumed to be continuous and linear. The values for the ice and snow thermal conductivity are taken from Yu and Rothrock (1996); Untersteiner (1961). As the optimization of the emission model lies beyond the scope of this work, we use the simplest setup variant of MILLAS consisting of a single layer of ice covered with a single layer of snow.

2.4 Simulation of Brightness Temperature of Rough Sea Ice

In the previous sections, we described the sea ice surface as composed of facets with orientation described by two angles: the slope α and the azimuthal direction γ . Subsequently, we analyzed the ALS data to extract information about statistical distributions of slopes and their orientation. ~~Finally, we conclude~~ We concluded that the exponential function is suitable to describe the probability density function of surface slopes for a range of ice surfaces with different degree of surface roughness.

In this section, we describe how we integrate the probability description of faceted sea ice surface with the MILLAS emission model. ~~To start, let's evoke the "global" coordination system in cartesian basis~~ We will start by describing the coordinate system that we used in the T_B simulations. The relations between radiometer antenna-look direction (\hat{r}) and the horizontal (\hat{h}) and vertical (\hat{v}) polarization vectors are described in Cartesian coordinate system. We show how these relation are represented in

the coordinate system associated with a facet. The vectors defined in the tilted facet coordinate system are denoted with the subscript i . Subsequently, we will derive the equation that sums up the emissions originating from multiple facets.

The Cartesian coordinate system $(\hat{x}, \hat{y}, \hat{z})$ in which with the origin in the center of the sensor footprint. In this reference frame the radiometer antenna-look direction (\hat{r}) is described as:

$$5 \quad \hat{r} = \hat{x} \sin(\theta_0) \cos(\phi_0) + \hat{y} \sin(\theta_0) \sin(\phi_0) - \hat{z} \cos(\theta_0), \quad (4)$$

where the θ_0 is the antenna incidence angle and the ϕ_0 is the azimuthal direction of the antenna, in this particular case we set the reference system so as $\phi_0 = 0$, and \hat{x} is parallel to the ground. The antenna setting defines the directions of the horizontal (\hat{h}) and vertical (\hat{v}) polarization vectors:

$$\hat{h} = -\hat{x} \sin(\phi_0) + \hat{y} \cos(\phi_0), \quad \hat{v} = -\hat{x} \cos(\theta_0) \cos(\phi_0) - \hat{y} \cos(\theta_0) \sin(\phi_0) - \hat{z} \sin(\theta_0). \quad (5)$$

10 ~~In order to unravel the relation~~ We are interested in finding a relationship between the radiation originating from a tilted face of the facet and the flat one, ~~we~~ For that purpose must consider the ~~“local”~~ “local”-tilted coordinate system associated with i -th facet (variables associated with individual facets are denoted with subscript i). The ~~local~~ local-z-coordinate in this tilted coordinate system is aligned with the facet normal vector \hat{n}_i , followed by \hat{x}_i and \hat{y}_i calculated accordingly:

$$\hat{z}_i = \hat{n}_i \quad \hat{y}_i = \frac{\hat{n}_i \times \hat{r}}{|\hat{n}_i \times \hat{r}|} \quad \hat{x}_i = \hat{y}_i \times \hat{z}_i \quad (6)$$

15 ~~The~~ Therefore the local incidence angle θ_i is ~~therefore calculated as~~ :

$$\theta_i = \cos^{-1}(-\hat{r} \cdot \hat{n}_i) \quad (7)$$

~~Thus and~~ Thus and the local horizontal and vertical polarization ~~vector are not aligned with the global ones~~ vectors:

$$\hat{h}_i = \hat{y}_i, \quad \hat{v}_i = -\hat{x}_i \cos(\theta_i) - \hat{z}_i \sin(\theta_i) \quad (8)$$

The emissions from the facet at an angle θ_i and polarization p are denoted with an asterisk: $T_B^*(\theta_i; p)$. In order to calculate the brightness temperatures observed in the global horizontal and vertical polarization it is necessary to account for the coordinates rotation (Ulaby, F. T. and Long, D. G. et al., 2014):

$$T_{Bi}(\theta_i; H) = (\hat{h} \cdot \hat{h}_i)^2 T_B^*(\theta_i; H) + (\hat{h} \cdot \hat{v}_i)^2 T_B^*(\theta_i; V) \quad (9a)$$

5

$$T_{Bi}(\theta_i; V) = (\hat{v} \cdot \hat{h}_i)^2 T_B^*(\theta_i; H) + (\hat{v} \cdot \hat{v}_i)^2 T_B^*(\theta_i; V) \quad (9b)$$

We model the sea ice surface as a set of facets, therefore the brightness temperature registered at the antenna aperture is a sum of contributions from N facets. We assume that each facet area A , at the distance R is visible at the incidence angle θ_i and covers a patch of antenna field of view, equal to the solid angle Ω_i :

$$10 \quad \Omega_i = \frac{A \cos(\theta_i)}{R^2 \cos(\alpha_i)} \quad (10)$$

The formula summing the contributions from N visible facets ~~also includes the antenna gain component ω_i~~ is:

$$T_B(\theta_0; p) = \frac{1}{N \cos(\theta_0)} \sum_{i=1}^N \omega_i T_{Bi}(\theta_i; p) \Omega_i \quad (11)$$

~~In~~ with ω_i the antenna gain component.

15 At this stage of our study we aim at modeling the surface roughness effect and for simplicity we assume a constant antenna gain effect of surface roughness on the T_B . As a first order approximation we assume that that antenna gain is constant across the whole field of view. ~~We also assume and~~ that the antenna is in a far field so the incidence θ_0 is assumed constant across the field of view. ~~These assumptions yield the final formula that was implemented~~ The resulting formula is:

$$T_B(\theta_0; p) = \frac{1}{N \cos(\theta_0)} \sum_{i=1}^N T_{Bi}(\theta_i; p) \sec(\alpha_i) (-\hat{r} \cdot \hat{n}_i) \quad (12)$$

This is the formula we implement in the geometrical roughness model:-

$$T_B(\theta_0; p) = \frac{1}{N \cos(\theta_0)} \sum_{i=1}^N T_{Bi}(\theta_i; p) \sec(\alpha_i) (-\hat{r} \cdot \hat{n}_i)$$

Figure 2.4 presents the data flow in the Geometrical Roughness Model that is used in modelling the emissions from rough sea ice surface geometrical roughness model. The model merges the emission model, in this case it is the MILLAS model the MILLAS emission model (suitable for sea ice,-) with the geometrical characterization of the faceted surface. The MILLAS emission model in In the presented setup the MILLAS emission model uses the sea ice surface temperature ($T_{surface}$), sea ice thickness (d_{ice}) and snow thickness (d_{snow}) as input variables. The geometrical optics GO part needs the cumulative probability distribution of surface slopes (CDF_α) and the antenna look direction (\hat{r}). The orientation of N facets representing the sea ice surface is calculated with the inverse transform sampling (ITS) Devroye (2006) (Devroye, 2006). This method returns a random slope value from a given non-uniform distribution, described by. The non-uniform distribution is described by a cumulative probability distribution, which in this case depends on the geometrical roughness parameter s_α . Similarly, the azimuthal angle γ_i is drawn from a uniform distribution. The result of this processing step is the set of N pairs of angles (α_i, γ_i) describing the orientation of N facets. In the next step, the local normal vector and the local incidence angle (θ_i) are calculated for each of the N facets. The θ_i is used for calculating the brightness temperature emitted from the i-th i-th facet with the emission model. The \hat{r} and the Shadowing occurs when $\theta_i > \pi/2$ and the radiation is emitted away from the antenna. In the current setup the double-bounce effects are not accounted for. \hat{r} and \hat{n}_i are used to calculate the local and global polarization directions, as well as the Ω_i . For the final step, the summed contributions from N facets are summed as in the equation 12. The result is the brightness temperature of the surface observed under θ_0 and polarization p.

The number of facets N is an adjustable parameter of the model. For the simulation results to be accurate and repeatable the value of N must be high enough, this however involves a trade-off with the computation time impacts on the quality of the simulation and the reproducibility of the results. In order to set the value of N we looked at the standard deviation of 20 simulations T_B simulations results for nadir and 45 degrees. We decided that the standard deviation of T_B should be lower than 0.1 K, as this is the accuracy of the EMIRAD-2 radiometer for the one second integration time. This criterion is met for N greater than 10^4 , which we take as the N value for further simulations.

3 Results

3.1 Brightness temperature simulations

In this section, we present the results of The three main results of this study are: (1) surface roughness reduced the polarization difference, this change is most pronounced at incidence angle greater than 50°, (2) nadir T_B is little affected and (3) comparison with the radiometer data and sensitivity study indicate that snow cover has greater impact on the T_B than surface roughness.

In section 3.1 we show the brightness temperature simulations for sea ice with different degree of large-scale surface roughness. The degree of roughness is parametrized by the probability distribution. To interpret the results we make a sensitivity analysis (section 3.2). The comparison of the simulated vs. measured T_B over 4.3 km flight track samples is shown in section 3.3.

5 3.1 Brightness temperature simulations

In section 2.2.2 we derived a parametrization of the degree of surface roughness. We approximate the roughness by exponential probability distribution function (PDF) of surface slopes. The shape of the PDF is fully described by the s_α parameter.

In our simulation s_α varies between ~~0.05 and 0.35, which is 2 and 20~~, in accordance with the measurements of surface slopes done during the SMOSice2014. As the aim of this study is to ~~single out~~ characterize the effect of surface roughness ~~, on L-band~~
10 T_B we keep the other ~~parameter~~ parameters in the emissivity model: surface temperature and ice and snow thickness constant ($T_{surface} = 260$ K, $d_{ice} = 1.42$ m, $d_{snow} =$ ~~0.14 m~~). ~~Further in this section, we will discuss the usage of other emissivity models.~~
The brightness temperatures are calculated for every degree of incidence angle in range 0-70 degrees. Figure 6 shows the simulation results. ~~Dashed lines mark the emissions from the specular surface, whereas the red and blue curves mark the emissions simulated from sea ice with different degree of surface roughness for vertical and horizontal polarizations,~~
15 ~~respectively. The intensity of the colour of the line corresponds to the roughness parameter used in the simulation.~~

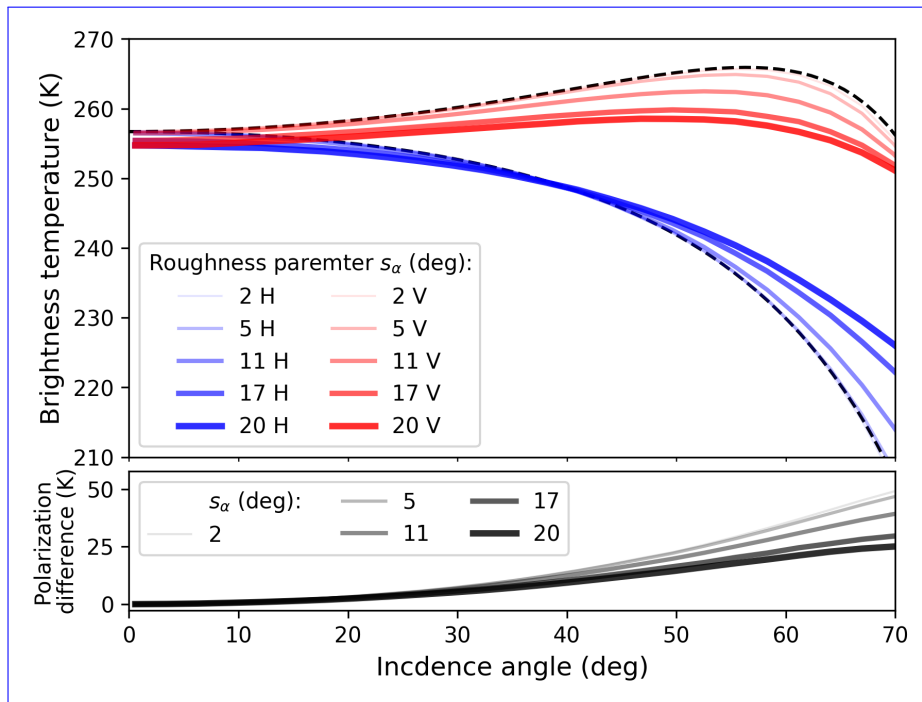


Figure 6. Effects of the large-scale surface roughness on the brightness temperature of sea ice, simulated with geometrical roughness model. Vertical polarization in red, horizontal in blue. The black dashed lines mark the T_B for the specular surface. The surface roughness parameter s_α varies between 0.05-2 to 0.3520, the thicker the line the higher the s_α . The inputs for the MILLAS emissivity model are kept constant: $T_{surface}=260$ K, $d_{ice}=1.42$ m, $d_{snow}=0.14$ m.

The effect of increasing surface roughness is two-fold. First, the polarization difference decreases as the horizontal and vertical polarization curves are brought together. Second, the overall near-nadir intensity is lowered by 2.6 K. The effect of roughness is more visible at higher incidence angles (60°). Second, the polarization difference decreases. For the highest value of the roughness parameter, vertical polarization decreases by 8 K, horizontal polarization experiences a 4 K increase. The effect of roughness is more pronounced for the higher larger values of roughness parameter s_α . This fact and is most visible at higher incidence angles (60°).

The polarization mixing can be explained by the approach used in this study. High values of s_α increase the emissions from the facet in horizontal (\hat{h}_i) and vertical (\hat{v}_i) polarizations are partially mixed when expressed in the (\hat{h}, \hat{v}) coordinate system (see eq. 12).

The lowering of the intensity has two possible explanations. First is that our model do not take into account shadowing effects. When local incidence angle is greater than 90° the facet is emitting away from the antenna. For the "near-nadir" angles (0-30°) the likelihood of encountering a large incidence angles in the inverse transform sampling shadowing is less than 1% for the most rough ice (see fig. 4).

Second explanation of this effect is associated with shape of the Fresnel curves. The polarization difference for these large incidence angles large incidence angles is larger than for the near-nadir ones, and the curve for vertical polarization is not

monotonic. After accounting for polarization rotation, in the summation over N facets, these height incidence angles are contributing more to. Therefore, the mean of the two polarizations ($T_B(\theta_0; H) + T_B(\theta_0; V)$)/2 i.e. total intensity) is fairly constant up to 30° and then drops sharply by 10 K by 60° . The trend continues for higher incidence angles. High values of s_α increase the likelihood of returning a large incidence angle in the inverse transform sampling. These large incidence angles contribute the overall lowering of the T_B . The contribution of this mechanism is ≈ 2 K for $T_B(0)$ in case of most rough ice. The 2 K estimate was obtained by integrating the drop in total intensity weighted by the PDF_α .

The above results are obtained with a Monte Carlo simulation. This method is a time consuming approach. Therefore, we propose a parametrization of the simulation results. The two effects: the polarization mixing and the lowering of brightness temperature, can be parametrized expressed in a fashion similar to the HQ model proposed by (Choudhury et al., 1979) Choudhury et al. (1979). Here we propose a formulation with two parameters H_α and Q_α .

$$T_B(\theta; p) = [(1 - Q_\alpha) \cdot T_B^*(\theta; p) + Q_\alpha T_B^*(\theta; q)] \cdot H_\alpha \quad (13)$$

where p and q stand for the polarization.

H_α accounts for the change in total intensity and Q_α for the polarization mixing. The emissions from the specular surface are denoted with an asterisk: $T_B^*(\theta; p/q)$. The proposed parametrization approximates the results obtained with the Monte Carlo simulation with a root mean square difference of 0.45 K

$$H_\alpha = a_1 s_\alpha^2 + a_0 \quad Q_\alpha = b_1 s_\alpha^2 + b_0 \quad (14)$$

where $a_1 = 0.020 \times 10^3$, $a_0 = 0.018 \times 10^{-3}$, $a_0 = 1$ and $b_1 = 0.537 \times 10^3$, $b_0 = 0.532 \times 10^{-3}$, $b_0 = 0$.

The emissions from the specular surface are an essential input for the geometrical roughness model used in this study. The exact shape of the simulated brightness temperature curves depends on the probability distribution of slopes, as well as on the emission characteristics of the specular surface. In this paragraph, we will investigate how the shape of the $T_B^*(\theta; p/q)$ influences the geometrical roughness model results. The shapes of the polarization curves i.e. the reflectivities for a given incidence angle, are described by the Fresnel equations. Equations that are determined by the permittivity of the medium (ϵ). (In this work we omit the question of penetration depth assuming the emissions are coming from the isothermal surface layer ice layer of constant permittivity). To investigate the impact of the varying ϵ we take a range of permittivities specific to sea ice, as calculated within the MILLAS model, as well as much higher permittivity corresponding to soil (30.6% sand, 55.9% silt, 13.5% clay) with different water content according to the model of (Mironov et al., 2015). These permittivities are used with the geometrical roughness model to simulate surfaces with different degree of surface roughness, described by s_α . Figures ??, ??, show the values of H_α and Q_α as a function of the surface roughness. In the present setup the sea ice permittivity depends on bulk ice salinity and ice temperature. We calculate the ϵ for a range of surface permittivities, ice temperatures ($250 \text{ K} < T_{ice} < 271 \text{ K}$) and salinities ($1 \text{ g/kg} < S_{ice} < 12 \text{ g/kg}$).

The sea ice permittivities from the MILLAS model range between $\epsilon = 3.1 + 0.05i$ (for $T_{ice} = 271 \text{ K}$, $S_{ice} = 7 \text{ g/kg}$) and $\epsilon = 4.6 + 0.8i$ (for $T_{ice} = 253 \text{ K}$, $S_{ice} = 1 \text{ g/kg}$), where T_{ice} is the bulk ice temperature and S_{ice} the bulk ice salinity. The curves corresponding to those values lie close together indicating that the proposed parametrization is suitable for all types of first year sea ice. As the permittivities are getting larger they affect the intensity parameter H_α . The H_α is close to 1 for $\epsilon \approx 19$, pass this value the H_α changes sign which corresponds to increase in $T_B(\theta; p/q)$. The effect of permittivity on the polarization mixing parameter (Q_α) is less pronounced. The dependence of the Q_α parameter on the roughness follows a similar quadratic curve regardless of the surface permittivity. It is important to remind that all those results were obtained with the surface slopes distribution derived from the ALS measurements specific to the different types of sea ice

3.2 Sensitivity analysis

In this section, we investigate the sensitivity of our model. This step will enable the interpretation of the results of the comparison between simulations and measurements presented in section 3.3. We start by estimating the sensitivity to sea ice contrition. Then we progress to analyze the model inputs: surface temperature, ice thickness, snow thickness, surface roughness.

The two most important factors influencing the L-band brightness temperature over sea ice are the ice concentration and the ice thickness. We calculate the sensitivity of our model to sea ice concentration by assuming a linear mixing of water and thick ice fractions within the radiometer footprint. The brightness temperature of sea water T_{Bw} (salinity of 33 g/kg, temperature 271.2 K) is approximately 110 K and $T_{Bi}(0, p/q)$ of thick sea ice ($T_{surf} = 260 \text{ K}$, $d_{ice} = 1.5 \text{ m}$, bulk salinity of 3 g/kg) is 240 K. The resulting sensitivity to sea ice concentration is $\approx 1.5 \text{ K}/\%$.

The sensitivity of the T_B to sea ice thickness over thin sea ice $d_{ice} < 0.75 \text{ m}$ is fundamental for the sea ice thickness retrieval from L-band radiometry. It is only when the sea ice thickness is significantly larger than the penetration depth of the L-band radiation when the T_{Bi} saturates. Therefore, in order to single out the contributions of surface roughness, our analysis is concentrated on sea ice thicker than 1 m.

Table 2 contains the sensitivities of the geometrical roughness model to the input parameters: roughness parameter s_{alpha} , ice thickness d_{ice} , snow thickness d_{snow} , surface temperature T_{surf} . Presented values are grouped into columns corresponding to the polarization and three incidence angles: 0° , 45° and 60° . The angles were chosen to reflect the antennae configuration during the SMOSice2014 with an additional 60° close to Brewster's angle where surface roughness effects are most pronounced.

Figures 7, 8 show the simulated L-band brightness temperature at 0° , 45° as a function of the surface temperature. In presented study we make considerable assumption about snow thickness. To illustrate the assumptions the plots are made for a range of snow thicknesses in corresponding line styles. In the MILLAS model, ice permittivity is parameterized with ice temperature. The non-monotonic shape of the curves is caused by change in ice permittivity. Therefore, in table 2 the relevant values of sensitivities are given for lower (250 K-265 K) and higher (265 K-270 K) temperature ranges.

The assumption about snow thickness has a considerable effect on the sea ice T_B (Maaß et al., 2013). For this reason the values of sensitivities are considered for a number of snow thickness values.

As far as the large-scale surface roughness is concerned the sensitivity increases almost linearly for the values of s_α between 0° and 20° which is the maximal value measured during the SMOSice2014 campaign.

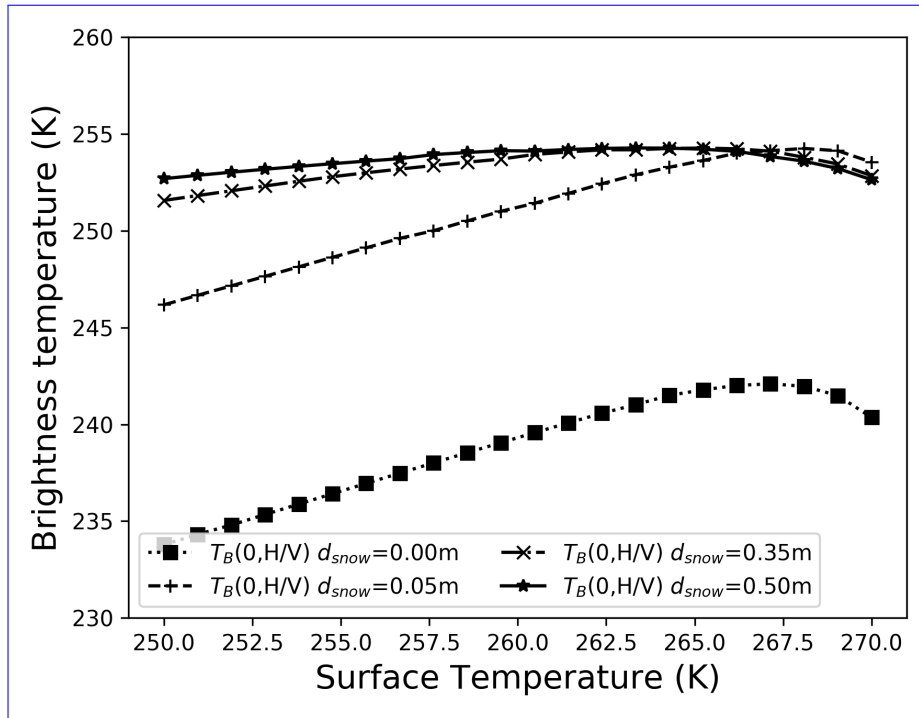
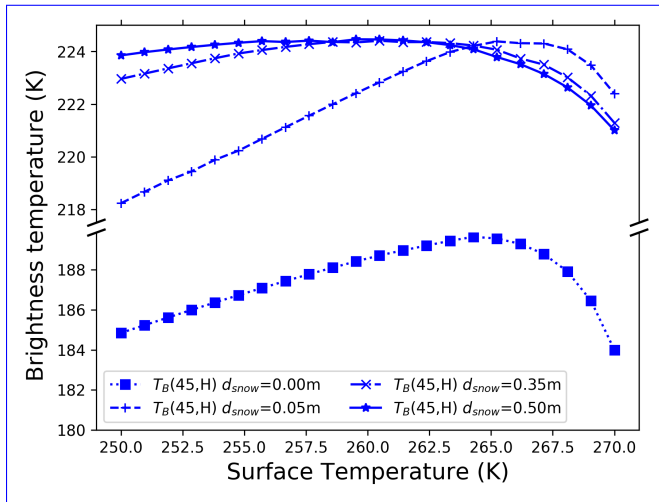


Figure 7. Change in the intensity parameter (H_α) nadir brightness temperature as predicted by the MILLAS emission model as a function of the roughness parameter s_α surface temperature. Curves corresponding to different surfaces with The different ϵ -specific line styles correspond to the water content m_w , are marked in colours different snow thickness assumptions. The calculation was done for sea ice thickness of one meter and surface roughness set to zero.

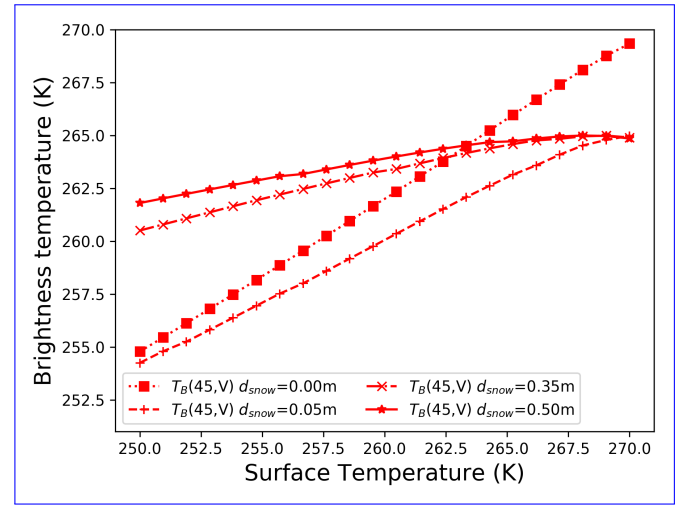
In order to interpret the results of the simulation-measurements comparison it is necessary to evaluate the uncertainties associated with the input parameters: surface temperature, ice thickness and snow thickness. In the following paragraphs we by "mean model sensitivity for the cold conditions" we understand the averaged absolute sensitivity for $T_B(0;H,V)$ and $T_B(45;H,V)$ at 250 K. We take the values for the lower temperature range as they reflect the conditions during SMOSice2014 campaign.

The surface temperature measurements done with the KT19.85 have an accuracy of 0.5 K. The mean surface temperature in the region covered by ice was 251.7 ± 3.5 K. We take the standard deviation of surface temperature measurements as the parameter uncertainty. Then we multiplied the parameter uncertainty by average absolute model sensitivity at low temperatures to obtain the model uncertainty associated with it. Thus, we estimate the uncertainties associated with surface temperature is 0.7 K.

The sea ice thickness measurements in this study are derived from the re-sampled ALS elevation data. The mean standard deviation of the re-sampled elevation measurements is 0.08 m. The assumption about the densities of snow, ice and water



(a) Change in the Horizontal polarization mixing parameter (Q_{α}) as a function of the roughness parameter s_{α} . Curves corresponding to different surfaces with different specific to the water content m_w , are marked in colours: incidence angle 45° : $T_B(45, H)$



(b) Vertical polarization, incidence angle 45° : $T_B(45, V)$

Figure 8. Change in the brightness temperature as predicted by the MILLAS emission model as a function of surface temperature. The different line styles correspond to the different snow thickness assumptions. The calculation was done for the sea ice thickness of one meter and surface roughness set to zero.

combined with the assumption on the snow thickness of 1/10 of ice thickness are leading to the uncertainty of 0.4 K. Therefore, taking into account the mean model sensitivity for the cold conditions prevailing during the flights we estimate the uncertainty associated with sea ice thickness is 0.5 K.

Unfortunately, the snow thickness measurements are not available. The snow layer although transparent for the L-band radiation is not invisible. The refraction on the snow-ice and snow-air interfaces alters the local incidence angles. Snow cover also has an effect on the temperature profile within the ice. This indirectly affects the permittivity of sea ice. All these factors make estimation of the uncertainty caused by snow thickness especially hard to quantify. We assume that snow thickness uncertainty is equal to mean standard deviation of the re-sampled elevation measurements, 0.08 m. The mean model sensitivity to snow thickness for the cold conditions is 8.6 K/m. Therefore, we estimate the uncertainty associated with snow thickness to be 0.7 K.

An important factor which is not directly included in the model is the sea ice concentration. In the model we assume the sea ice concentration to be 100% in order to single out the much smaller contribution of surface roughness. However, if a linear mixing model is applied the sensitivity to sea ice contraction is -1.5 K/%. During the pre-processing of the airborne laser scanner (ALS) data we excluded the seventy meter sections with more than 5% missing values. The missing values are caused by the instrument setup (rotating mirror, edge of swath) or by lack of return reflection from open water or thin ice. We estimate that the uncertainty associated with the sea ice concentration is up to 7.5 K.

Table 2. Table with sensitivities of the brightness temperature at nadir, 45° and 60° as simulated with Geometrical Optics surface roughness model. The input parameters: roughness parameter s_{α} , ice thickness d_{ice} , snow thickness d_{snow} , surface temperature T_{surf} .

	$T_B(0; H, V)(K)$		$T_B(45; H)(K)$		$T_B(45; V)(K)$		$T_B(60; H)(K)$		$T_B(60; V)(K)$	
$\frac{\partial}{\partial s_{\alpha}} _{d_{snow}=0}$	-0.01 to -0.20		0.06 to 0.80		-0.08 to -1.20		0.11 to 1.70		-0.14 to -2.10	
$\frac{\partial}{\partial s_{\alpha}} _{d_{snow}=0.1m}$	-0.01 to -0.21		0.02 to 0.30		-0.05 to -0.74		0.05 to 0.77		-0.08 to -1.19	
$\frac{\partial}{\partial s_{\alpha}} _{d_{snow}=0.25m}$	-0.01 to -0.21		0.02 to 0.33		-0.05 to -0.76		0.05 to 0.80		-0.14 to -1.22	
$\frac{\partial}{\partial s_{\alpha}} _{d_{snow}=0.35m}$	-0.01 to -0.21		0.02 to 0.34		-0.05 to -0.77		0.05 to 0.82		-0.14 to -1.24	
$\frac{\partial}{\partial s_{\alpha}} _{d_{snow}=0.45m}$	-0.01 to -0.21		0.02 to 0.35		-0.05 to -0.78		0.05 to 0.83		-0.14 to -1.25	
$\frac{\partial}{\partial s_{\alpha}} _{d_{snow}=0.5m}$	-0.01 to -0.21		0.02 to 0.37		-0.05 to -0.79		0.05 to 0.85		-0.14 to -1.26	
range (K)	250-265	265-270	250-265	265-270	250-265	265-270	250-265	265-270	250-265	265-270
$\frac{\partial}{\partial d_{ice}}$	-0.91	2.05	0.18	3.49	-1.77	0.16	0.58	3.28	-2.12	-1.24
$\frac{\partial}{\partial d_{snow}}$	8.51	-2.03	6.58	-3.18	10.71	0.23	5.68	-2.45	10.10	0.89
$\frac{\partial}{\partial T_{surf}} _{d_{snow}=0}$	0.50	-0.43	0.4	-0.95	0.61	0.15	0.29	-1.32	0.69	0.66
$\frac{\partial}{\partial T_{surf}} _{d_{snow}=0.1m}$	0.34	-0.23	0.3	-0.5	0.41	0.02	0.26	-0.63	0.44	0.19
$\frac{\partial}{\partial T_{surf}} _{d_{snow}=0.25m}$	0.18	-0.38	0.12	-0.59	0.24	-0.11	0.09	-0.68	0.27	0.05
$\frac{\partial}{\partial T_{surf}} _{d_{snow}=0.35m}$	0.11	-0.39	0.05	-0.61	0.17	-0.16	0.01	-0.66	0.21	-0.01
$\frac{\partial}{\partial T_{surf}} _{d_{snow}=0.45m}$	0.06	-0.40	0.01	-0.58	0.13	-0.19	-0.03	-0.67	0.17	-0.05
$\frac{\partial}{\partial T_{surf}} _{d_{snow}=0.5m}$	0.05	-0.40	0.01	-0.57	0.11	-0.19	-0.05	-0.66	0.15	-0.06

To put the partial sensitivity in to perspective, the expected changes in the T_B caused by the strongest surface roughness during measured during SMOSIce2014 campaign do not exceed -2.2 K for nadir and 1 K and -5.6 K for the horizontal and vertical polarization of the 45° antenna, respectively.

To conclude, the sensitivity analysis of geometrical roughness model leads to the conclusion that on the scale of one radiometer footprint (70 m) the surface roughness effects will be hard to observe in the SMOSIce2014 flights data.

3.3 Simulations vs. Measurements

In this section, we compare the brightness temperature measured with the EMIRAD-2 radiometer with brightness temperature simulations. The comparison is done on 4.3 km section as to justify the assumption of the isotropic azimuth distribution. We want to determine the simulation setup that is best in reproducing best reproduces the radiometer measurements. And whether the inclusion of the surface roughness in the simulation brings significant improvement. The limitation of this approach is that

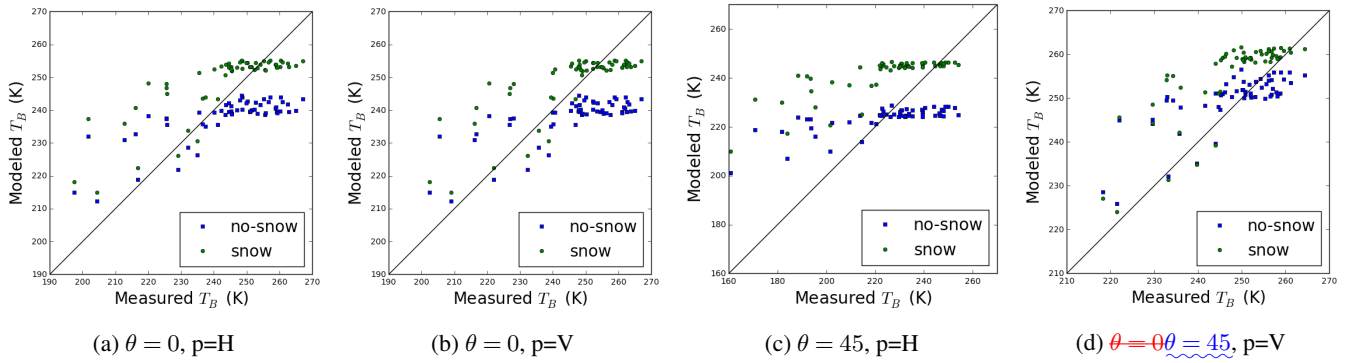


Figure 9. Scatter-plots illustrating the comparisons between the EMIRAD-2 data and the T_B simulated without GO roughness included - **specular**. Results corresponding to the setup with snow are marked in green, without snow in blue.

we assume the ice observed by [the](#) side looking antenna and the ice below the flight path have the same properties. We consider the surface temperature, the sea ice thickness and the surface roughness along the flight and we use them to run the statistical roughness model, described [earlier with a in section 2.4 with](#) MILLAS single ice layer setup as the brightness temperature module. [When needed-In setups including snow layer,](#) the snow thickness is set to be 10% of the sea ice thickness. The calculation is done for [60 s](#) averages, during which the aircraft covers the distance of approximately [4.3 km](#). For each channel we made four simulation setups, two without roughness: Flat no- snow, Flat snow, and two with roughness included: Rough (GO) no-snow, Rough (GO) snow. As for the performance metrics of the model setups, we use the coefficient of determination (r^2), the root-mean-square error (RMSE), the bias and unbiased root- mean-square error (ubRMSE). These metrics are widely used in the assessment of the performance of satellite measurements [Entekhabi et al. \(2010\)](#) ([Entekhabi et al., 2010](#)). Table 3 holds the results of the comparison expressed in terms of r^2 , RMSE, bias and ubRMSE. The corresponding scatter-plots illustrating the comparison between measured and modeled brightness temperatures are presented on the Figure 10.

The values of r^2 for all “channel - simulation setup” combinations do not exceed 0.3. The simplified one-layer model managed to capture only 30% of the signal variance even with surface roughness included. Furthermore, the inclusion of surface roughness brings little improvement to the statistics. In case of vertical polarization, where the model studies indicate the most sensitivity to roughness, the r^2 is even a little lower. The inclusion of a very crude snow thickness parametrization is more successful in capturing the radiometer measurements variability. All metrics show the four model setups perform poorly in reproducing the EMIRAD-2 measurements. The bias is the lowest for the side-looking vertical channel ([to up to 5 K](#)). For the nadir channel the inclusion of snow in the model reduces the bias by [11 K](#) to the value of [1.5 K](#). For the horizontal polarization channel the inclusion of snow has an opposite effect, changing the absolute value of bias from [to 4.6 K](#) to [-13.2 K](#). The high values of RMSE and ubRMSE show a general miss-fit of the model to the data.

[The results of the comparison are also presented in the form of histograms of the difference between the measured and simulated \$T_B\$ \(figure 11\). For all four antenna feeds the difference between simulated and measured \$T_B\$ decreases whenever the setups include snow.](#)

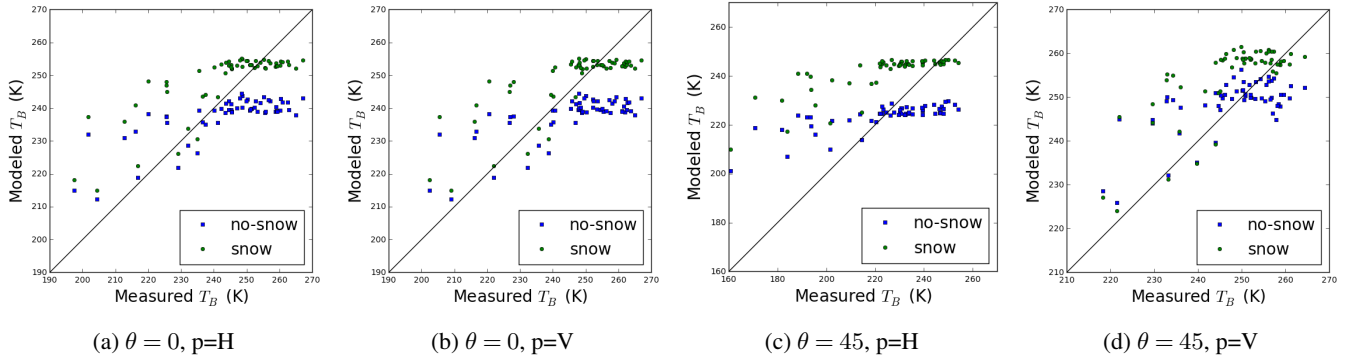


Figure 10. Scatter-plots illustrating the comparisons between the EMIRAD-2 data and the T_B simulated **with GO roughness included**. Results corresponding to the setup with snow are marked in green, without snow in blue.

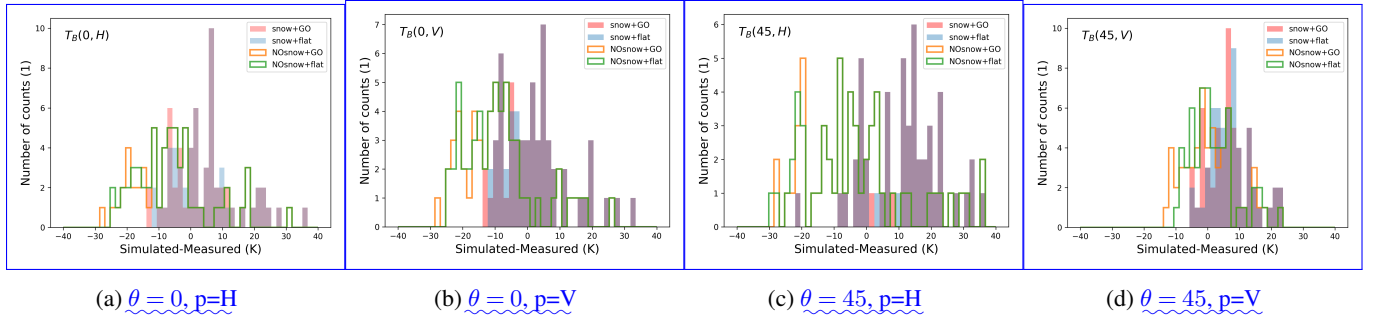


Figure 11. Histograms of the differences between the EMIRAD2 measurements and simulation setups for four antenna feeds.

4 Discussion and Conclusions

In this paper we ~~have addressed the issue~~ address the knowledge gap concerning the influence of the decimetre-scale surface roughness ~~influence~~ on the L band brightness temperature of sea ice. We used the airborne laser scanner (ALS) data to characterize the sea ice surface and to produce the digital elevation model (DEM) of the sea ice surface. From the DEM we derived the probability distribution of surface slopes (α) and their azimuthal orientation (γ). We found that the probability distribution function of α (PDF_α) can be described with an exponential function regardless of the degree of roughness of sea ice surface. The exponent parameter (s_α) is a quasi-quadratic function of the standard deviation of surface heights. In the second part of this work we used the PDF_α in the Monte Carlo simulation of the emission from a faceted sea ice surface. The effect of surface roughness is little noticeable in near-nadir, accounting for up to ~~of decrees~~ 2.6 K decreases in T_B . The polarization curves around Brewster's angle are most affected. The vertical polarization ~~is decreased by~~ decreases by 8 K and horizontal polarization ~~increased by~~ increases by 4 K for the roughest ice, compared with the specular sea ice surface. The effect of large-scale surface roughness on polarization curves is not linear with the degree of the surface roughness described by s_α . Meaning that the alteration of the T_B curves is ~~stronger~~ strongest for the roughest surface. The overall change of emission due to the

Table 3. Performance of the different T_B simulation setups in terms of coefficient of determination r^2 , RMSE [K], bias [K], ubRMSE [K]. For EMIRAD-2 channels four model setups are tested: Flat no snow, Flat snow, Rough no snow, Rough snow. Nadir-looking antenna channels are treated together.

		r^2	RMSE (K)	bias (K)	ubRMSE (K)
$T_B, \theta = 0^\circ$	Flat, no snow	0.21	30.9	12.6	27.8
	Flat, snow	0.29	26.1	1.3	26.7
	Rough, no snow	0.20	30.8	12.5	27.8
	Rough, snow	0.29	26.2	1.5	26.1
$T_B H, \theta = 40^\circ$	Flat, no snow	0.22	29.9	4.6	29.5
	Flat, snow	0.30	30.3	-13.2	27.3
	Rough, no snow	0.22	29.8	4.5	29.4
	Rough, snow	0.30	30.3	-13.2	27.3
$T_B V, \theta = 40^\circ$	Flat, no snow	0.16	29.1	4.0	28.9
	Flat, snow	0.24	27.2	-1.9	27.1
	Rough, no snow	0.15	29.3	5.0	28.9
	Rough, snow	0.22	27.1	-1.2	27.1

Performance of the different T_B

simulation setups in terms of coefficient of determination r^2 , RMSE K, bias K, ubRMSE K. For EMIRAD-2 channels four model setups are tested: Flat no snow, Flat snow, Rough no snow, Rough snow. Nadir-looking antenna channels are treated together.

large-scale surface roughness can be expressed as a superposition of change in intensity (H_α) and an increase in polarization mixing (Q_α). The change in intensity depends primarily on the surface permittivity, whereas the polarization mixing shows little dependence on ϵ . The parametrization is suitable for all types of sea ice. However, the ~~changes in this parameterization are negligible for all types of first-year ice~~ sensitivity analysis demonstrates that the expected change in T_B is comparable in

5 magnitude to the uncertainty associated with the model input parameters.

The results have implication for the current and future L-band missions. The operational SMOS sea ice thickness product relies on near-nadir T_B observations (0-30°), therefore the large scale surface roughness will have little effect on the retrieval. Especially as the method is used with thin sea ice which tends to be smooth. While the SMAP and CIMR missions, which operate at incidence angles of 40° and 55°, respectively, are more exposed to the surface roughness effects. However, as the

10 effect on vertical polarization is stronger than on horizontal polarization, for SMAP $T_B(40, H)$ the influence is close to zero.

Lastly, we compared the simulation of the brightness temperature with and without surface roughness with the radiometer measurements. Unfortunately, this ~~had shown that one layer setup of the emission showed that our~~ model is not ~~enough to capture capturing~~ the brightness temperature variability at the scale of ~~60 seconds (flight track)~~ 4.3 km flight track. The

inclusion of surface roughness ~~has proven is~~ less important than the inclusion of a crude snow thickness parameterization. ~~The~~ This is confirmed by the sensitivity analysis of the model. Another possible explanation is that the sea ice in the studied region was highly heterogeneous in ~~term of its permittivity and thickness. Therefore a better~~ terms of its thickness and snow cover. Furthermore, a simple two-layer emission model used in this study has its limitations in capturing the T_B variability. Better result might be obtained if a multi-layer model together with the snow thickness measurements is used. With such setup the direct inclusion of sea ice facets orientation in the radiometer field of view ~~was used~~ will be a valuable option to improve the T_B simulation. This however, would require in-situ measurements of sea ice permittivity, snow thickness, temperature and roughness ~~Thus the author's recommendation for the~~ as well as detailed characterization of the antenna gain. Thus the authors recommendation for future studies is to measure the microphysical snow and sea ice properties together with surface roughness directly in the radiometer's field of view.

Code and data availability. Code and data are available from the authors on request.

Author contributions. Conceptualization, M.Miernecki and L.Kaleschke; Methodology, M.Miernecki; Software, M.Miernecki and N.N.Maaß; Validation, M.Miernecki, N.Maaß; Formal Analysis, M.Miernecki and L.Kaleschke; Investigation, M.Miernecki; Resources, L.Kaleschke; Data Curation, S.Hendricks, S.S.Søbjrg; Writing—Original Draft Preparation, M.Miernecki; Writing—Review & Editing, L.Kaleschke, N.Maaß; Visualization, M.Miernecki; Supervision, L.Kaleschke; Project Administration, L.Kaleschke; Funding Acquisition, L.Kaleschke

This research was funded by the HGF Alliance, Remote Sensing and Earth System Dynamics. The European Space Agency co-financed the AWI research aircraft Polar 5 and helicopter flights (ESA contract 4000110477/14/NL/FF/lf; PI S.Hendricks) and the development and validation of SMOS sea ice thickness retrieval methods (ESA contracts 4000101476/10/NL/CT and 4000112022/14/I-AM; PI L.Kaleschke). Technical University of Denmark (DTU) co-financed and conducted the measurements with EMIRAD2 L-band radiometer on Polar 5.

Competing interests. The authors declare no conflict of interest. The founding sponsors had no role in the design of the study; in the collection, analyses, or interpretation of data; in the writing of the manuscript, and in the decision to publish the results

Acknowledgements. The authors acknowledge the institutions providing the data and people involved in carrying out the measurements. The TerraSAR-X and TanDEM-X teams provided the SAR data for this study.

The following abbreviations are used in this manuscript:

ALS	airborne Laser Scanner
CDF	Cumulative Distribution Function
DEM	Digital Elevation Model
GO	Geometrical Optics
ITS	Inverse Transform Sampling
MILLAS	Microwave L-band LAyered Sea ice emission model
PDF	Probability Distribution Function
RFI	Radio Frequency Interference
SAR	Synthetic Aperture Radar
SMOS	Soil Moisture and Ocean Salinity
T_B	brightness temperature

References

- Balling, J. E., Søbjaerg, S. S., Kristensen, S. S., and Skou, N.: RFI detected by kurtosis and polarimetry: Performance comparison based on airborne campaign data, in: 2012 12th Specialist Meeting on Microwave Radiometry and Remote Sensing of the Environment, MicroRad 2012 - Proceedings, 2012.
- 5 Beckers, J. F., Renner, A. H. H., Spreen, G., Gerland, S., and Haas, C.: Sea-ice surface roughness estimates from airborne laser scanner and laser altimeter observations in Fram Strait and north of Svalbard, *Annals of Glaciology*, 56, 235–244, <https://doi.org/https://doi.org/10.3189/2015AoG69A717>, 2015.
- Burke, W. J., Schmugge, T., and Paris, J. F.: COMPARISON OF 2.8- AND 21-cm MICROWAVE RADIOMETER OBSERVATIONS OVER SOILS WITH EMISSION MODEL CALCULATIONS., *J Geophys Res*, 84, 287–294, <https://doi.org/10.1029/JC084iC01p00287>, 1979.
- 10 Choudhury, B. J., Schmugge, T. J., Chang, A., and Newton, R. W.: EFFECT OF SURFACE ROUGHNESS ON THE MICROWAVE EMISSION FROM SOILS., *Journal of Geophysical Research*, 84, 5699–5706, <https://doi.org/10.1029/JC084iC09p05699>, 1979.
- Cox, G. F. and Weeks, W. F.: Salinity variations in sea ice, *Journal of Glaciology*, 13, 109–120, 1974.
- Cox, G. F. N. and Weeks, W. F.: EQUATIONS FOR DETERMINING THE GAS AND BRINE VOLUMES IN SEA ICE SAMPLES., CRREL Report (US Army Cold Regions Research and Engineering Laboratory), 1982.
- 15 Devroye, L.: Chapter 4 Nonuniform Random Variate Generation, in: *Simulation*, edited by Henderson, S. G. and Nelson, B. L., vol. 13 of *Handbooks in Operations Research and Management Science*, p. pp. 83–121, Elsevier, [https://doi.org/10.1016/S0927-0507\(06\)13004-2](https://doi.org/10.1016/S0927-0507(06)13004-2), 2006.
- Dierking, W.: Laser profiling of the ice surface topography during the Winter Weddel Gyre Study 1992, *Journal of Geophysical Research*, 100, 4807–4820, 1995.
- 20 Dierking, W.: RMS slope of exponentially correlated surface roughness for radar applications, *IEEE Transactions on Geoscience and Remote Sensing*, 38, 1451–1454, <https://doi.org/10.1109/36.843040>, 2000.
- Entekhabi, D., Reichle, H. R., Koster, D. R., and Crow, T. W.: Performance metrics for soil moisture retrievals and application requirements, *Journal of Hydrometeorology*, 11, 832–840, <https://doi.org/http://dx.doi.org/10.1175/2010JHM1223.1>, 2010.
- Hendricks, S., Steinhage, D., Helm, V., Birnbaum, G., Skou, N., Kristensen, S., Søbjaerg, S., Gerland, S., Spreen, G., Bra-trein, M., and King, J.: SMOSice 2014: Data acquisition report, Tech. rep., <https://earth.esa.int/web/guest/campaignsProject:Technicalsupportforthe2014SMOSicecampaigninSESvalbardESAcontractnumber:4000110477/14/NL/FF/fftechnicalreportNo.1,2014,2014>.
- Huntemann, M., Heygster, G., Kaleschke, L., Krumpen, T., Mäkynen, M., and Drusch, M.: Empirical sea ice thickness retrieval during the freeze-up period from SMOS high incident angle observations, *Cryosphere*, 8, 439–451, <https://doi.org/10.5194/tc-8-439-2014>, 2014.
- 30 Kaleschke, L., Tian-Kunze, X., Maaß, N., Beitsch, A., Wernecke, A., Miernecki, M., Müller, G., Fock, B. H., Gierisch, A. M. U., Schlünzen, K. H., Pohlmann, T., Dobrynin, M., Hendricks, S., Asseng, J., Gerdes, R., Jochmann, P., Reimer, N., Holfort, J., Melsheimer, C., Heygster, G., Spreen, G., Gerland, S., King, J., Skou, N., Søbjaerg, S. S., Haas, C., Richter, F., and Casal, T.: SMOS sea ice product: Operational application and validation in the Barents Sea marginal ice zone, *Remote Sensing of Environment*, 180, 264–273, <https://doi.org/http://doi.org/10.1016/j.rse.2016.03.009>, 2016.
- 35 Ketchum, R.: Airborne laser profiling of the arctic pack ice, *Remote Sensing of Environment*, 2, 41–52, 1971.
- Klein, L. and Swift, C.: An improved model for the dielectric constant of sea water at microwave frequencies, *IEEE Transactions on Antennas and Propagation*, 25, 104–111, <https://doi.org/10.1109/TAP.1977.1141539>, 1977.

- Landy, J., Isleifson, D., Komarov, A., and Barber, D.: Parameterization of Centimeter-Scale Sea Ice Surface Roughness Using Terrestrial LiDAR, *Geoscience and Remote Sensing, IEEE Transactions on*, 53, 1271–1286, <https://doi.org/10.1109/TGRS.2014.2336833>, 2015.
- Lawrence, H., Demontoux, F., Wigneron, J. P., Paillou, P., Wu, T. D., and Kerr, Y. H.: Evaluation of a Numerical Modeling Approach Based on the Finite-Element Method for Calculating the Rough Surface Scattering and Emission of a Soil Layer, *IEEE Geoscience and Remote Sensing Letters*, 8, 953–957, <https://doi.org/10.1109/LGRS.2011.2131633>, 2011.
- Lawrence, H., Wigneron, J. ., Demontoux, F., Mialon, A., and Kerr, Y. H.: Evaluating the semiempirical H-Q model used to calculate the L-band emissivity of a rough bare soil, *IEEE Transactions on Geoscience and Remote Sensing*, 51, 4075–4084, <https://doi.org/10.1109/TGRS.2012.2226995>, 2013.
- Liu, C., Chao, J., Gu, W., Li, L., and Xu, Y.: On the surface roughness characteristics of the land fast sea-ice in the Bohai Sea, *Acta Oceanologica Sinica*, 33, 97–106, <https://doi.org/10.1007/s13131-014-0509-3>, 2014.
- Maaß, N., Kaleschke, L., Tian-Kunze, X., and Drusch, M.: Snow thickness retrieval over thick Arctic sea ice using SMOS satellite data, *Cryosphere*, 7, 1971–1989, <https://doi.org/10.5194/tc-7-1971-2013>, 2013.
- Matzler, C. and Standley, A.: Relief effects for passive microwave remote sensing, *International Journal of Remote Sensing*, 21, 2403–2412, <https://doi.org/10.1080/01431160050030538>, 2000.
- 15 Mironov, V. L., Kerr, Y. H., Kosolapova, L. G., Savin, I. V., and Muzalevskiy, K. V.: A Temperature-Dependent Dielectric Model for Thawed and Frozen Organic Soil at 1.4 GHz, *IEEE Journal of Selected Topics in Applied Earth Observations and Remote Sensing*, 8, 4470–4477, <https://doi.org/10.1109/JSTARS.2015.2442295>, 2015.
- Mäkynen, M., Cheng, B., and Similä, M.: On the accuracy of thin-ice thickness retrieval using MODIS thermal imagery over Arctic first-year ice, *Annals of Glaciology*, 54, 87–96, <https://doi.org/10.3189/2013AoG62A166>, 2013.
- 20 Panofsky, H. A. and Brier, G. W.: Some applications of statistics to meteorology, Pennsylvania State University Press, 1958.
- Prigent, C. and Abba, P.: Sea surface equivalent brightness temperature at millimeter wavelengths, *Annales Geophysicae [0992-7689]*, 8, 627–634, 1990.
- Ricker, R., Hendricks, S., Helm, V., Skourup, H., and Davidson, M.: Sensitivity of CryoSat-2 Arctic sea-ice freeboard and thickness on radar-waveform interpretation, *Cryosphere*, 8, 1607–1622, <https://doi.org/10.5194/tc-8-1607-2014>, 2014.
- 25 Søbjaerg, S., Kristensen, S., Balling, J., and Skou, N.: The airborne EMIRAD L-band radiometer system, pp. 1900–1903, <https://doi.org/10.1109/IGARSS.2013.6723175>, 2013.
- Stroeve, J. C., Markus, T., Maslanik, J. A., Cavalieri, D. J., Gasiewski, A. J., Heinrichs, J. F., Holmgren, J., Perovich, D. K., and Sturm, M.: Impact of surface roughness on AMSR-E sea ice products, *IEEE Transactions on Geoscience and Remote Sensing*, 44, 3103–3116, <https://doi.org/10.1109/TGRS.2006.880619>, 2006.
- 30 Strübing, K. and Schwarz, J.: Die Eisverhältnisse in der Barentssee während der IRO-2-Testfahrt mit R/V Lance 17. – 27.03.2014, Tech. rep., abschlussbericht vorgelegt von JS Consulting, Großhansdorf, im Auftrag des AWI, Bestellnummer 12/45086354 zum Werkvertrag Vor-/Nachbereitung und Durchführung der IRO-2-Testfahrt im Rahmen des Vorhabens Entwicklung und Optimierung eines Ozean-Meereis Vorhersagemodells für das Nordpolarmeer, BMWi-Förderkennzeichen: 03SX328H, 2014.
- Tian-Kunze, X., Kaleschke, L., Maaß, N., Mäkynen, M., Serra, N., Drusch, M., and Krumpfen, T.: SMOS-derived thin sea ice thickness: Algorithm baseline, product specifications and initial verification, *Cryosphere*, 8, 997–1018, <https://doi.org/10.5194/tc-8-997-2014>, 2014.
- 35 Tiuri, M. E., Sihvola, A. H., Nyfors, E. G., and Hallikaiken, M. T.: The Complex Dielectric Constant of Snow at Microwave Frequencies, *IEEE Journal of Oceanic Engineering*, 9, 377–382, <https://doi.org/10.1109/JOE.1984.1145645>, 1984.

- Ulaby, F. T. and Long, D. G., Blackwell, W. J., Elachi, C., Fung, A. K., Ruf, C., Sarabandi, K., Zebker, H. A., and Van Zyl, J.: Microwave radar and radiometric remote sensing, University of Michigan Press Ann Arbor, 2014.
- Untersteiner, N.: On the mass and heat budget of arctic sea ice, *Archiv für Meteorologie, Geophysik und Bioklimatologie Serie A*, 12, 151–182, 1961.
- 5 Vant, M. R., Ramseier, R. O., and Makios, V.: The complex-dielectric constant of sea ice at frequencies in the range 0.1-40 GHz, *Journal of Applied Physics*, 49, 1264–1280, 1978.
- Warren, S. G., Rigor, I. G., Untersteiner, N., Radionov, V. F., Bryazgin, N. N., Aleksandrov, Y. I., and Colony, R.: Snow depth on Arctic sea ice, *Journal of Climate*, 12, 1814–1829, [https://doi.org/10.1175/1520-0442\(1999\)012<1814:SDOASI>2.0.CO;2](https://doi.org/10.1175/1520-0442(1999)012<1814:SDOASI>2.0.CO;2), 1999.
- Yu, Y. and Rothrock, D. A.: Thin ice thickness from satellite thermal imagery, *Journal of Geophysical Research C: Oceans*, 101, 25 753–
10 25 766, <https://doi.org/10.1029/96JC02242>, 1996.